Inorganic Chemistry

Article

pubs.acs.org/IC

Mn(II)-Based Porous Metal–Organic Framework Showing Metamagnetic Properties and High Hydrogen Adsorption at Low Pressure

Zheng-Bo Han,*[,†] Rui-Yun Lu,[†] Yan-Fang Liang,[†] Yan-Ling Zhou,[‡] Qing Chen,[‡] and Ming-Hua Zeng*[,‡]

[†]College of Chemistry, Liaoning University, Shenyang 110036 P. R. China

[‡]Key Laboratory for the Chemistry and Molecular Engineering of Medicinal Resources (Ministry of Education), School of Chemistry and Chemical Engineering, Guangxi Normal University, Guilin 541004, P. R. China

Supporting Information

ABSTRACT: A Mn(II)-based homometallic porous metal–organic framework, $Mn_5(btac)_4(\mu_3\text{-}OH)_2(EtOH)_2\cdot DMF\cdot 3EtOH\cdot 3H_2O$ (**1**, btac = benzotriazole-5-carboxylate), has been solvothermally synthesized and structurally characterized by elemental analysis, thermogravimetric analysis, and X-ray crystallographic study. **1** is a 3D neutral framework featuring 1D porous channels constructed by $\{Mn-OH-Mn\}_n$ chains and btac linkers. Magnetic studies show that **1** is a 3D metamagnet containing 1D $\{Mn-OH-Mn\}_n$ ferrimagnetic chains. High-pressure H_2 adsorption measurement at 77 K reveals that activated **1** can absorb 0.99 wt % H_2 at 0.5 atm and reaches a maximum of 1.03 wt % at 5.5 atm. The steep H_2 absorption at lower pressure (98.2% of the storage capacity at 0.5 atm) is higher than the corresponding values of some MOFs (MIL-100 (16.1%), MOF-177 (57.1%), and MOF-5 (22.2%)). Furthermore, activated **1** can adsorb CO_2 at room temperature and 275 K. The adsorption enthalpy is 22.0 kJ mol^{-1}, which reveals the high binding ability for CO_2. Detailed gas sorption implies that the exposed Mn(II) coordination sites in the activated **1** play an important role to improve its adsorption capacities.

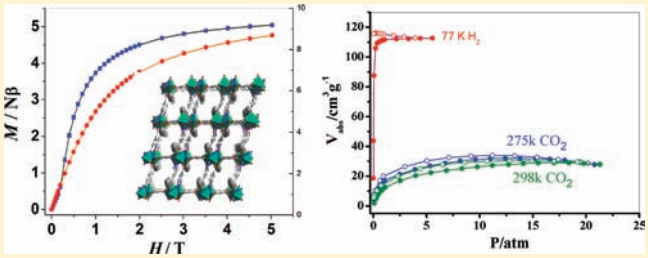

INTRODUCTION

Porous metal–organic frameworks (MOFs) have attracted great interest, not only because of their versatile intriguing architectures but also because of their potential applications as functional materials.[1−3] The design and construction of functional porous MOFs with additional physical properties, such as magnetism, is a challenge because it is difficult to obtain simultaneously larger pore sizes and relatively strong magnetic interactions.[4] The porosity usually depends on the use of relatively long bridging ligands. However, magnetic superexchange requires relatively short exchange pathways between two adjacent metal centers. In general, these multifunctional MOFs have usually been focused on two general synthetic strategies: (1) Using a stable organic radical ligand link to the adjacent metal centers to build porous hybrid skeleton;[5] (2) using topological magnetic chains or clusters connected by longer organic linkers to form a porous open framework.[6] Several hydroxide-bridged porous coordination polymers have been reported,[2a,b,7] which show interesting magnetic properties.

Organic carboxylate ligands have been widely used in synthesizing porous MOFs[8] or magnetic materials[9] with esthetical topologies and unusual properties because of the controllable length of ligand and the various coordination modes of the carboxyl group. Because the conditions of noncompensation of the individual spin moments are generally difficult to achieve in 3D homometallic systems, the 3D homometallic systems containing ferrimagnetic behaviors have been rarely reported.[10] Herein, we present a study of a 3D homometallic porous MOF, $Mn_5(btac)_4(\mu_3\text{-}OH)_2(EtOH)_2\cdot DMF\cdot 3EtOH\cdot 3H_2O$ (**1**), (btac = benzotriazole-5-carboxylate), with metamagnetic properties, containing ferrimagnetic chains and high H_2 adsorption ability at low pressure.

EXPERIMENTAL SECTION

Materials and Methods. All chemicals for synthesis were commercially available reagents of analytical grade and were used without further purification. The C, H, and N microanalyses were carried out with Perkin-Elmer 240 elemental analyzer. The FT-IR spectra were recorded from KBr pellets in the 4000−400 cm^{-1} range on a Nicolet 5DX spectrometer. Thermogravimetric analyses (TGA) were taken on a Perkin-Elmer Pyrisl (25−600 °C, 5 °C min^{-1}, flowing N_2(g)). Powder X-ray diffraction (PXRD) analyses were recorded with a Bruker AXS D8 advanced automated diffractometer with Cu Kα radiation. Gas sorption isotherms were performed with a Belsorp-Max automatic volumetric adsorption apparatus. A sample of **1** was soaked with CH_2Cl_2 for 24 h. After the removal of CH_2Cl_2 by decanting, the sample was dried under dynamic vacuum (<10^{-3} Torr) at room temperature (25 °C) overnight. Before the measurement, the sample

Received: October 10, 2011
Published: December 5, 2011

was dried again by using the "outgas" function of the surface area analyzer for 4 h at 150 °C. The detailed ac and dc magnetic data were collected on a Quantum Design MPMS SQUID-XL-5 magnetometer using the crushed single-crystal samples. Magnetic data were corrected for the diamagnetic contribution calculated from Pascal constants[11] and a background of the sample holder.

Solvothermal Synthesis. *$Mn_5(btac)_4(\mu_3\text{-}OH)_2(EtOH)_2\cdot DMF\cdot 3EtOH\cdot 3H_2O$ (1).* A reaction mixture of $Mn(CH_3COO)_2\cdot 4H_2O$ (0.5 mmol, 0.123 g), H_2btac (0.4 mmol, 0.065 g), DMF (4 mL), and EtOH (4 mL) was stirred for 20 min in air, then transferred and sealed in a 18-mL Teflon-lined autoclave, which was heated in an oven to 473 K for 72 h, followed by slow cooling (5 K h^{-1}). The resulting light yellow crystals were washed with distilled water and dried in air (yield: ca. 33%). Elemental analysis calcd (%) for **1** $C_{41}H_{57}Mn_5N_{13}O_{19}$: C, 37.57; H, 4.38; N, 13.89. Found: C, 37.83; H, 4.41; N, 13.68%. IR (KBr pellets, cm^{-1}): 3429 (m), 1595 (s), 1558 (s), 1476 (w), 1401 (s), 1308 (vs), 1196 (s), 784 (s).

X-ray Crystallography. Crystallographic data of **1** were collected at 173 K with a Apex II diffractometer with Mo Kα radiation (λ = 0.71073 Å) and graphite monochromator using the ω-scan mode. The structure was solved by direct methods and refined on F^2 by full-matrix least-squares, using SHELXTL.[12] Crystallographic data and experimental details for structural analyses are summarized in Table 1. The selected bond lengths and bond angles are listed in Table 2. The CCDC reference number is 823231 for **1**. A copy of the data can be obtained free of charge on application to CCDC, 12 Union Road, Cambridge CB2 1EZ, UK [Fax: int code +44(1223)336−033. E-mail: deposit@ccdc.cam.ac.uk].

Table 1. Crystal Data and Structure Refinement for 1

$Mn_5(btac)_4(\mu_3\text{-}OH)_2(EtOH)_2\cdot DMF\cdot 3EtOH\cdot 3H_2O$ (**1**)	
empirical formula	$C_{41}H_{57}Mn_5N_{13}O_{19}$
Fw	1310.70
crystal system	triclinic
space group	$P\bar{1}$
a (Å)	11.105(1)
b (Å)	12.577(1)
c (Å)	20.075(2)
α (deg)	82.840(1)
β (deg)	77.765(2)
γ (deg)	79.258(1)
V (Å^3)	2681.5(4)
ρ_{calcd}(mg/cm^{-3})	1.623
μ (mm^{-1})	1.229
F(000)	1342
Z	2
θ for data collection (deg)	1.04−26.00
collected reflections	14 749
Independent reflections(R_{int})	10 362(0.0191)
R indices [I > 2σ (I)] [a]	0.0730
wR indices (all data)	0.2117
goodness-of-fit on F^2	1.062
largest diff. peak and hole (e Å^{-3})	2.468 and −2.254

[a] $R_1 = \sum||F_o| - |F_c||/\sum|F_o|$; $wR_2 = \sum[w(F_o^2 - F_c^2)^2]/\sum[w(F_o^2)^2]^{1/2}$

RESULTS AND DISCUSSION

Solvothermal reaction of $Mn(CH_3COO)_2\cdot 4H_2O$ and H_2btac in the presence of DMF and EtOH leads to the generation of light yellow crystals with an overall formula of $Mn_5(btac)_4(\mu_3\text{-}OH)_2(EtOH)_2\cdot DMF\cdot 3EtOH\cdot 3H_2O$ (**1**), which was determined based on an X-ray single-crystal diffraction, elemental analysis, and TGA. Compared with the large amount of reported metal-carboxylate complexes, only one complex with btac ligand, $[Co_3(OH)(btac)_2]\cdot 3.7H_2O$, has been reported,[10b] which shows different structure.

Table 2. Selected Bond Lengths (Å) and Angles (deg) for 1[a]

Mn(1)−N(1B)	2.227(4)	Mn(1)−N(10)	2.229(4)
Mn(1)−O(12)	2.231(3)	Mn(1)−O(11)	2.236(3)
Mn(1)−N(6A)	2.239(4)	Mn(1)−N(9)	2.240(4)
Mn(2)−O(4)	2.108(3)	Mn(2)−O(7C)	2.147(4)
Mn(2)−O(11)	2.217(3)	Mn(2)−N(8)	2.246(4)
Mn(2)−N(5A)	2.269(4)	Mn(3)−O(5D)	2.092(3)
Mn(3)−O(9)	2.103(3)	Mn(3)−O(2A)	2.147(3)
Mn(3)−N(4A)	2.186(4)	Mn(3)−O(10)	2.222(3)
Mn(4)−O(8C)	2.101(3)	Mn(4)−O(10)	2.111(3)
Mn(4)−N(3)	2.176(4)	Mn(4)−O(9)	2.246(3)
Mn(5)−O(1A)	2.110(4)	Mn(5)−O(9)	2.146(3)
Mn(5)−O(6D)	2.177(3)	Mn(5)−O(12E)	2.201(3)
Mn(5)−N(2)	2.259(4)	Mn(5)−N(11E)	2.263(4)
Mn(5)−O(12)−Mn(1)	107.7(1)	O(10)−Mn(4)−O(9)	78.47(11)
Mn(2)−O(11)−Mn(1)	108.26(13)	Mn(2)−O(10)−Mn(3)	113.87(13)
Mn(4)−O(10)−Mn(2)	102.80(13)	Mn(4)−O(10)−Mn(3)	101.35(12)
Mn(3)−O(9)−Mn(5)	104.43(13)	Mn(3)−O(9)−Mn(4)	100.93(12)

[a] Symmetry operation: *A* $x-1, y, z$; *B* $x, y-1, z$; *C* $-x+1, -y+1, z$; *D* $-x+1, -y+1, -z+1$; *E* $x, y+1, z$.

Crystal structure. X-ray crystallography revealed that **1**, crystallized in the space group $P\bar{1}$, exhibited an interesting 3D porous metal−organic framework constructed by pentanuclear Mn(II) subunits and btac bridges. The asymmetric unit consists of five Mn(II) ions, four btac ligands, two μ_3-OH groups, two coordinated EtOH molecules, and some solvent molecules located in the crystal lattice. The Mn(1) atom is six-coordinated by four nitrogen atoms from four different btac ligands and two oxygen atoms from two individual EtOH molecules to form a distorted octahedral geometry. Mn(2) and Mn(5) are also six-coordinated and surrounded by two nitrogen atoms from two different btac ligands and four oxygen atoms from two distinct btac ligands, one EtOH molecule and one μ_3-OH group. Unlike Mn(1), Mn(2), and Mn(5), Mn(3) and Mn(4) are five-coordinated and surrounded by four oxygen atoms and one nitrogen atom from three individual btac ligands and two μ_3-OH groups, forming a trigonal bipyramidal geometry (Figure 1). The btac ligand has two types of different bridging modes: one adopts μ_5 bridging mode through three btac nitrogen atoms and μ_2,η_2-carboxylate group (Scheme 1a), another adopts μ_4-bridging mode through two btac nitrogen atoms and μ_2,η_2-carboxylate group (Scheme 1b). Thus, Mn(1) is linked to Mn(2) *via* two −N−N− bridges and a μ_2-OH of EtOH, Mn(2) is linked to Mn(3) through one −N−N− bridge and one μ_3-OH bridge, Mn(2) is linked to Mn(4) through two *syn-syn* μ_2-carboxylate bridges and one μ_3-OH bridge, Mn(3) is linked to Mn(4) through two μ_3-OH bridges, Mn(4) is linked to Mn(5) through one −N−N− bridge and one μ_3-OH bridge, Mn(3) is linked to Mn(5) through two *syn-syn* μ_2-carboxylate bridges and one μ_3-OH bridge, forming a pentanuclear Mn(II) subunit with the Mn−O−Mn angle ranging from 101.4 to 113.9°. The pentanuclear Mn(II) subunits are further connected through μ_3-OH groups to form a extended {Mn−OH−Mn}$_n$ chain (Figure 2). Furthermore, the extended infinite chains were connected by btac ligands to form a 3D porous MOF (Figure 3a). The solvent-accessible volume of the

dx.doi.org/10.1021/ic2021929 | Inorg. Chem. 2012, 51, 674−679

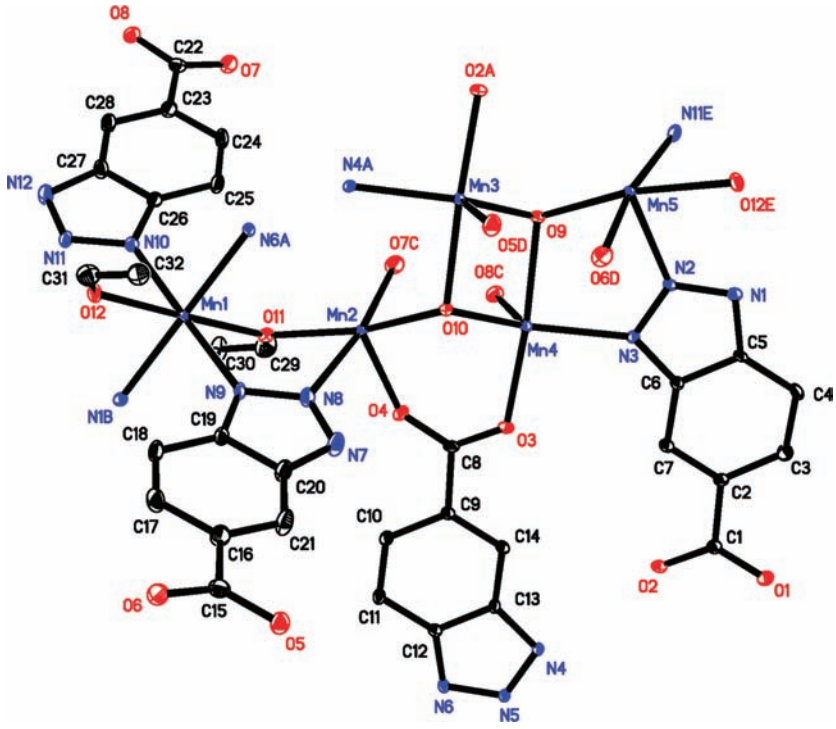

Figure 1. Coordination environment of the Mn(II) centers in **1**. Symmetry transformations used to generate equivalent atoms: *A* $x-1, y, z$; *B* $x, y-1, z$; *C* $-x+1, -y+1, -z$; *D* $-x+1, -y+1, -z+1$; *E* $x, y+1, z$.

Scheme 1. Coordination Modes of btac in 1

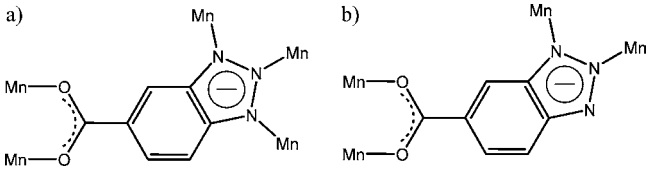

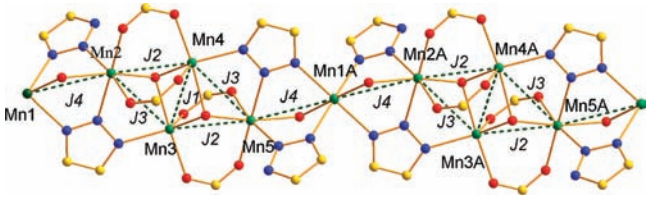

Figure 2. Spin topology of homometallic ferrimagnetic chain.

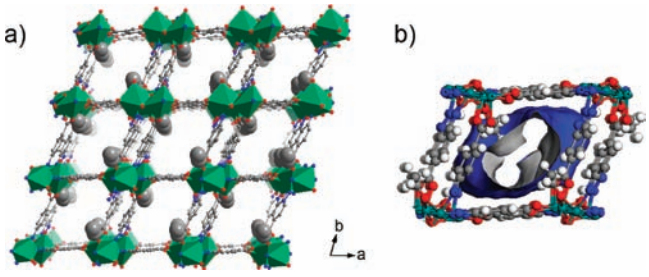

Figure 3. (a) View of 3D metal organic framework in **1**, in which C atoms of EtOH molecules are highlighted in the space-filling model. (b) Enlarged image of the micropore.

unit cell was estimated (PLATON program[13]) to be 1080.9 Å^3, which accommodates lattice solvent molecules, and is approximately 40.3% of the unit-cell volume (2681.5 Å^3). The 1D pore exhibits a dumbbell-type channel with a size of 9.6 × 7.8 Å (atom to atom distance, or 8.8 × 7.5 Å, excluding van der Waals radii,[14] Figure 3b). This is even larger than the reported pore size (7.2 × 5.7 Å) of MAF-25,[15] which shows gas separation for N_2, H_2, and CO_2. Compared with the previously reported Co(II)-btac compound,[10b] Co(II) centers are bridged by μ_3-OH groups to form a $Co_3(OH)_2$ chain, then are linked by btac ligands in the μ_5 mode to form a 3D porous MOF.

Thermal Stability. The TGA curve (Figure S1 in the Supporting Information) of **1** shows that the weight loss of the guest and coordinated solvent molecules was well resolved. The first step from 25 to 140 °C with ca. 19.9% loss may be attributed to the loss of guest molecules (the weight ca. 20.2%) (step I) and the 7.3% loss corresponds to the release of two coordinated EtOH molecules (step II) up to ~201 °C (ca. 7.1%). The PXRD patterns of **1** (Figure 4) show that the diffraction patterns are almost the same as the simulated ones, indicating the phase purity of the products. The differences in intensity may be due to the preferred orientation of the powder samples.[16] The PXRD patterns of dehydrated samples and the desolvated (EtOH) samples after gas sorption experiments have been also measured and compared with that of **1**. The PXRD pattern of dehydrated samples (after heating at 110 °C under vacuum for 4 h) is almost the same as that of the as-synthesized **1**, confirming the framework is stable after losing the lattice water and solvent molecules. However, the PXRD pattern of the desolvated samples (under vacuum at 150 °C for 4 h) after gas sorption exhibits a decrease in intensity, and the position of partial peaks change, suggesting that a crystal of the coordination network was gradually distorted as a result of the crystal transformation after the loss of coordinated EtOH molecules.[17] TGA performed on the desolvated samples after gas sorption experiments showed insignificant weight loss (~1%) up to 200 °C, confirming that all guest molecules and coordinated solvents were removed from the pores of **1** (Figure

dx.doi.org/10.1021/ic2021929 | *Inorg. Chem.* 2012, 51, 674–679

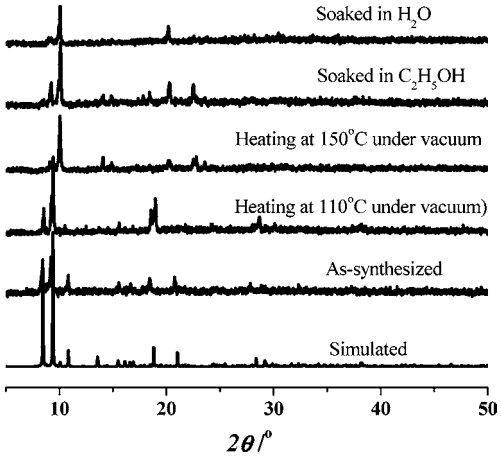

Figure 4. XRPD patterns of simulated, as-synthesized, and immersed dried crystals for 24 h in different solvents.

S2 in the Supporting Information). To examine if the framework can be recovered after the loss of the guest and coordinated solvent molecules, a crystalline sample of **1** was dried under vacuum at 150 °C for 4 h and then immersed in water and wet ethanol. The PXRD patterns of samples immersed in ethanol or water are almost the same as those of the dried samples under vacuum at 150 °C for 4 h, indicating that the framework change is an irreversible process after guest molecules and coordinated EtOH molecules removed.

Magnetic Properties. The magnetic susceptibility per Mn_5 unit measured on a polycrystalline sample of **1** under an applied field of 10 kOe is shown in Figure 5. The value of $\chi_m T$ at 300 K is 18.23 cm^3 K mol^{-1}, which is lower than the spin-only value of 21.83 cm^3 K mol^{-1} magnetically five isolated high-spin Mn(II) ions ($S = {}^5/_2$, $g = 2.0$), indicating the presence of a dominant antiferromagnetic interaction. Upon cooling, the $\chi_m T$ product first decreases smoothly to a rounded minimum (5.82 cm^3 K mol^{-1}) at 20 K; then, there is an abrupt increase to 9.08 cm^3 K mol^{-1} at 4.0 K, and finally, $\chi_m T$ values again decrease to 2.4 cm^3 K mol^{-1} at 2 K. From 4 to 2 K, the decreasing experimental $\chi_m T$ may be due to interchain antiferromagnetic interactions and/or the saturation effect. This feature is similar to that reported by Cao et al. for a similar 3D complex containing 1D chains and is the typical signature of the so-called topological ferrimagnetism.[10b] The temperature dependence of the reciprocal susceptibility above 70 K follows the Curie–Weiss law with a Weiss constant of $\theta = -95$ K, further confirming dominant antiferromagnetic interactions between Mn(II) ions. The full hydration and the full dehydration of $Mn_5(btac)_4(\mu_3\text{-}OH)_2(EtOH)_2\cdot DMF\cdot 3EtOH\cdot 3H_2O$ do not influence the magnetic properties (Tc, Weiss constant) (Figure S3 in the Supporting Information).

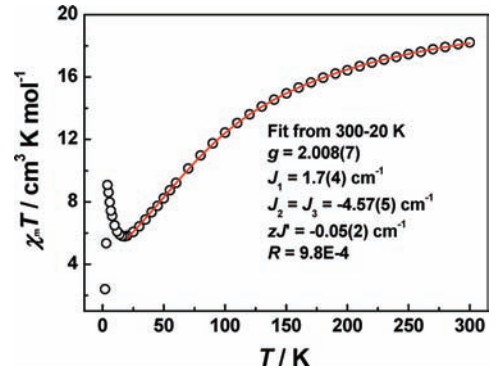

Figure 5. Plots of $\chi_m T$ versus T for the polycrystalline samples of **1**(○) with solid lines showing the theoretical fit to the experimental data.

The magnetic behaviors of **1** are further characterized by field-dependent measurements at low temperature (Figure 6).

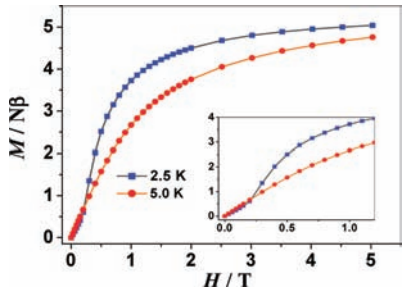

Figure 6. Magnetization curves at 2.5 K and 5 K. The inset is a blow-up of the low field region.

The sigmoidal shape of the $M-H$ curve at 2 K clearly indicates the field-induced transition from an antiferromagnetic to a paramagnet state, which is characteristic of a metamagnet. The critical field is 3000 Oe, estimated as the field at which a maximum dM/dH value is reached. Upon increasing the field above the critical field, the magnetization increases and saturates rapidly. The saturation magnetization is 5.03 $N\beta$, confirming the $S = {}^5/_2$ ground state for a pentanuclear unit, which mainly arises from three Mn(II) moments that are antiparallel to those of two other Mn(II) within the chain to give the ferrimagnetic chain, and the resultant of one chain is opposite to that of neighboring ones to give the final antiferromagnetic interactions. As expected, the sigmoidal feature of the magnetization curve disappears at 5 K, which is above the critical temperature for 3D antiferromagnetic ordering. Further measurements revealed that **1** is a soft magnet without detectable magnetic hysteresis. The temperature dependence of the ac magnetic susceptibility is also measured and confirms the occurrence of the magnetic ordering at 3.0 K, at which only χ' (the in-phase component) reach maximum value. No resolving out-of-phase signal and frequency dependence were observed (Figure S4 in the Supporting Information).

1 is unusual example of a 3D metamagnet containing 1D ferrimagnetic chains. According to the ferrimagnetic behavior and the chain topology of **1**, we can determine the spin topology of the chain and the nature of the magnetic interactions through different bridges. There are four sets of magnetic exchange pathways within the chain: (1) consisting of two −N−N− bridges from a μ_4-btac group and a μ_5-btac group and a μ_2-OH bridge from a EtOH ligand (J_1); (2) consisting of one −N−N− bridge from a μ_5-btac group and a μ_3-OH bridge (J_2), (3) consisting of one *syn-syn* μ_2-1,3-carboxylate bridge and a μ_3-OH bridge (J_3), and (4) consisting of two μ_3-OH bridges (J_4). It is well-known that compared with the μ_2-O bridge, *syn-syn* carboxylate bridges and double-atom bridges such as −N−N− play a negligible role in mediating the magnetic exchanges. Therefore, the magnetic exchange within the Mn−O−Mn is dominant. The Mn−O−Mn angles within and between the pentamers are 101.4–113.9° and 107.7° respectively, which

dx.doi.org/10.1021/ic2021929 | Inorg. Chem. 2012, 51, 674–679

favor antiferromagnetic couplings between the Mn(II) ions.[10a,18]

Prior to this study, no analytical expression was available for determining the exchange parameters in a 1D Heisenberg ferrimagnet consisting of alternating interactions. Furthermore, the Bonner and Fisher numerical computation method,[19] based on rings of increasing size, is not useful here because the number of required spins $S = {}^5/_2$ lies outside the range of computational possibilities. Given the spin value, a convenient expression may be deduced from a classical spin model, using the spin Hamiltonian

$$H = -J_1\Sigma S_{5i+2}S_{5i+1} - J_2\Sigma(S_{5i+3}S_{5i+1} + S_{5i+2}S_{5i}) - J_3\Sigma(S_{5i+3}S_{5i+2} + S_{5i+1}S_{5i}) - J_4\Sigma(S_{5i+2}S_{5i+4} + S_{5i-1}S_{5i})$$

where J_1, J_2, J_3, and J_4 stand for the exchange interactions and where the S_n are classical spin vectors. This approximation is fully justifiable when studying manganese(II) chains that exhibit large spins, $S = {}^5/_2$. A least-squares fit of the observed magnetic data was made, and a set of parameters, $g = 2.008$, $J_1 = 1.7$ cm^{-1}, and $J_2 = J_3 = -4.7$ cm^{-1}, was obtained. These could explain the overall antiferromagnetic behavior of **1**. Noting that the asymmetric unit of **1** contains odd numbers of Mn(II) ions, the antiferromagnetically interacted Mn(II) ions should result in an uncompensated net magnetic moment within the pentamers, thus leading to a ferrimagnetic chain. This phenomenon has been found in a few other homometallic systems with an odd number of interacting metal ions.[10a,18]

Gas Adsorption. To check the porosity of activated **1**, H_2 adsorption studies were carried out at 77 K. As shown in Figure 7, the steep increase in H_2 uptake at low-pressures (110 cm^3(STP)/g, 0.99 wt % at ca. 0.5 atm and 112 cm^3(STP)/g, 1.01 wt % at ca. 1 atm) and a maximum capacity of 114 cm^3(STP)/g (1.03 wt %) at 5.5 atm was observed. The adsorption and desorption are not reversible, which is different from a lot of other MOFs in H_2 adsorption.[20] Such desorption kinetics might attributed to the removal of bound EtOH molecules and the exposed Mn(II) coordination sites that are generated in the desolvated samples. Moreover, the rapid increase in H_2 uptake at low-pressures implies a strong interaction between H_2 and the exposed metal centers.[21] Chen and co-workers have revealed that the removal of axial water ligands from paddle-wheel secondary building units (SBUs) by thermal activation exposes the metal binding sites in MOF-505;[22] Long et al. have shown a similar phenomenon in a MOF with tetrazolate ligands.[23] The H_2 molecules proved to be bound strongly with these exposed metal sites; therefore, the incorporation of an accessible unsaturated metal center has been shown to be a viable strategy to increase H_2 adsorption affinity.[24] In addition, benzene rings in the organic linkers also play an important role for H_2 adsorption.[25] As in the case of the MOF-5 and IRMOF-8 reported by Yaghi et al., their different adsorption abilities may be attributed to differences in the organic ligands that have been considered as significant adsorption sites.[26] These results reveal that the MOFs that possess more aromatic rings in the organic ligands could enhance the H_2 storage capacities.[27] Therefore, the rapid increase in H_2 uptake at low-pressures may result from the presence of exposed Mn(II) sites and the double-walled linkers exist in **1**.

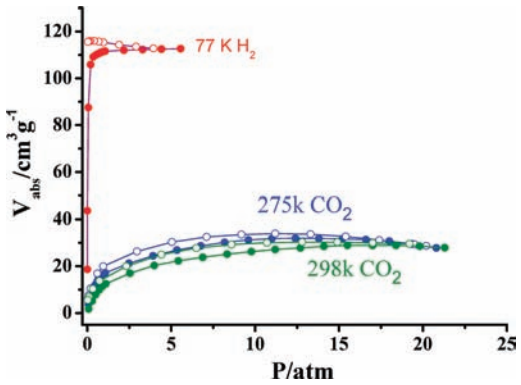

Figure 7. Gas adsorption isotherms of the activated **1**: CO_2 at 275 K and H_2 at 77 K.

Although the maximum uptake of H_2 is relatively low in comparison to the high capacity coordination framework reported to date,[28] the H_2 uptake of **1** at low pressures (1.01 wt %, 1 atm) is comparable to that of IRMOF-1,[29] but lower than that of Cu_2(BPTC), which displays high capacities of H_2 uptake (~2.47 wt %) under similar conditions (77 K and 1 atm). At 0.5 atm, 98.2% of the H_2 storage capacity of **1** has been reached, which is higher than those for some porous materials that have been reported to be promising for the H_2 storage: MIL-100 (16.1%), MOF-177 (57.1%), and MOF-5 (22.2%).[30]

For further study of the gas sorption, CO_2 adsorption was measured (Figure 7) at 275 and 298 K. CO_2 adsorption gave maximum CO_2 uptake of 32.3 cm^3 (STP)/g (11.0 atm, 275 K) and 29.0 cm^3 (STP)/g (15.5 atm, 298 K), respectively. Virial analysis[24] of the CO_2 adsorption isotherms revealed that the isosteric heat of adsorption of **1** at zero surface coverage is 22.0 kJ mol^{-1}, which implies that the activated **1** has higher binding ability to CO_2. The observed value (22 kJ mol^{-1}) is similar to that of HKUST-1 with unsaturated metal sites, exhibiting enthalpies in the low coverage region of around 35 kJ mol^{-1}.[31]

The phenomenon may be caused by a direct interaction between CO_2 and the exposed unsaturated metal centers where CO_2 is end-on coordinated to the manganese ion of the framework.[32]

CONCLUSION

In conclusion, a porous Mn(II) MOF (**1**) based on Mn_5 subunits and btac bridges has been successfully synthesized. Detailed magnetic measures show that **1** exhibits 3D metamagetic properties with homometallic ferrimagnetic chains. In addition, H_2 and CO_2 adsorption properties on the activated **1** were also explored, which prove that the introduction of the metal active sites and/or double-walled linkers to the activated MOFs makes a positive effect on the gas adsorption.

ASSOCIATED CONTENT

Supporting Information

TGA curve, additional magnetic data, and crystallographic data (CIF) for **1**. This material is available free of charge via the Internet at http://pubs.acs.org.

AUTHOR INFORMATION

Corresponding Authors

*E-mail: ceshzb@lnu.edu.cn (Z.-B.H.).
*E-mail: zmh@mailbox.gxnu.edu.cn (M.-H.Z.).

■ ACKNOWLEDGMENTS

This work was granted financial support from National Natural Science Foundation of China (Grant No. 20871063 and 91022015) and the Program for New Century Excellent Talents at the University of the Ministry of Education China (NCET-07-217).

■ REFERENCES

(1) (a) Furukawa, H.; Ko, N.; Go, Y. B.; Aratani, N.; Choi, S. B.; Choi, E.; Yazaydin, A. O.; Snurr, R. Q.; O'Keeffe, M.; Kim, J.; Yaghi, O. M. *Science* **2010**, *239*, 424−428. (b) Li, J.-R.; Kuppler, R. J.; Zhou, H.-C. *Chem. Soc. Rev.* **2009**, *38*, 1477−1504. (c) Zhang, Y.-B.; Zhang, W.-X.; Feng, F.-Y.; Zhang, J.-P.; Chen, X.-M. *Angew. Chem., Int. Ed.* **2009**, *48*, 5287−5290. (d) Zeng, M.-H.; Yao, M.-X.; Liang, H.; Zhang, W.-X.; Chen, X.-M. *Angew. Chem., Int. Ed.* **2007**, *46*, 1832−1835.

(2) (a) Kurmoo, M. *Chem. Soc. Rev.* **2009**, *38*, 1353−1379. (b) Kurmoo, M.; Kumagai, H.; Chapman, K. W.; Kepert, C. J. *Chem. Commun.* **2005**, 3012−3014. (c) Chen, Q.; Zeng, M. H.; Zhou, Y. L.; Kurmoo, M. *Chem. Mater.* **2010**, *22*, 2114−2119. (d) Zhang, Z. M.; Yao, S.; Li, Y. G.; Clérac, R.; Lu, Y.; Su, Z. M.; Wang, E. B. *J. Am. Chem. Soc.* **2009**, *131*, 14600−14601.

(3) (a) Seo, J. S.; Whang, D.; Lee, H.; Jun, S. I.; Oh, J.; Jeon, Y. J.; Kim, K. *Nature* **2000**, *404*, 982−986. (b) Zheng, Y.-Z.; Tong, M.-L.; Zhang, W.-X.; Chen, X.-M. *Angew. Chem., Int. Ed.* **2006**, *45*, 6310−6314.

(4) (a) Kepert, C. J. *Chem. Commun.* **2006**, 695−700. (b) Férey, G. *Nat. Mater.* **2003**, *2*, 136−137.

(5) Maspoch, D.; Ruiz-Molina, D.; Wurst, K.; Domingo, N.; Cavallini, M.; Biscarini, F.; Tejada, J.; Rovira, C.; Veciana, J. *Nat. Mater.* **2003**, *2*, 190−195.

(6) (a) Masciocchi, N.; Galli, S.; Colombo, V.; Maspero, A.; Palmisano, G.; Seyyedi, B.; Lamberti, C.; Bordiga, S. *J. Am. Chem. Soc.* **2010**, *132*, 7902−7904. (b) Han, Z. B.; Zhang, G. X.; Zeng, M. H.; Ge, C. H.; Zou, X. H.; Han, G. X. *CrystEngComm* **2009**, *11*, 2629−1633.

(7) (a) Kurmoo, M.; Kumagai, H.; Akita-Tanaka, M.; Inoue, K.; Takagi, S. *Inorg. Chem.* **2006**, *45*, 1627−1637. (b) Wang, Z.; Zhang, B.; Fujiwara, H.; Kobayashi, H.; Kurmoo, M. *Chem. Commun.* **2004**, 416−417. (c) Rujiwatra, A.; Kepert, C. J.; Claridge, J. B.; Rosseinsky, M. J.; Kumagai, H.; Kurmoo, M. *J. Am. Chem. Soc.* **2001**, *123*, 10584−10594.

(8) Yuan, D.; Zhao, D.; Sun, D.; Zhou, H.-C. *Angew. Chem., Int. Ed.* **2010**, *49*, 5357−5361.

(9) (a) Han, Z.-B.; Zhang, G.-X.; Zeng, M.-H.; Yuan, D.-Q.; Fang, Q.-R.; Li, J.-R.; Ribas, J.; Zhou, H.-C. *Inorg. Chem.* **2010**, *49*, 769−771. (b) Han, Z.-B.; Ji, J.-W.; An, H.-Y.; Zhang, W.; Han, G.-X.; Zhang, G.-X.; Yang, L.-G. *Dalton Trans.* **2009**, 9807−9811.

(10) (a) Wang, R. H.; Gao, E. Q.; Hong, M. C.; Gao, S.; Luo, J. H.; Lin, Z. Z.; Han, L.; Cao, R. *Inorg. Chem.* **2003**, *42*, 5486−5488. (b) Zhang, X.-M.; Hao, Z.-M.; Zhang, W.-X.; Chen, X.-M. *Angew. Chem., Int. Ed.* **2007**, *46*, 3456−3459.

(11) Kahn, O. *Molecular Magnetism*; VCH: NewYork, 1993.

(12) Sheldrick, G. M. *SHELXTL*, Version 6.10; Bruker Analytical X-ray Systems: Madison, WI, 2001.

(13) Spek, A. L.*PLATON*, A. M. C. T.; Utrecht University: Utrecht, The Netherlands, 1998.

(14) Bondi, A. *J. Phys. Chem.* **1964**, *68*, 441−453.

(15) Lin, J. B.; Zhang, J. P.; Chen, X. M. *J. Am. Chem. Soc.* **2010**, *132*, 6654−6656.

(16) Gilbert, A.; Baggott, J. *Essentials of Molecular Photochemistry*; CRC Press: Boca Raton, FL, 1991; pp 87−89.

(17) Zeng, M.-H.; Hu, S.; Chen, Q.; Xie, G.; Shuai, Q.; Gao, S.-L.; Tang, L.-Y. *Inorg. Chem.* **2009**, *48*, 7070−7079.

(18) Jia, H.-P.; Li, W.; Ju, Z.-F.; Zhang, J. *Dalton Trans.* **2007**, 3699−3704.

(19) Bonner, J. C.; Fisher, M. E. *Phys. Rev. A: At., Mol., Opt. Phys.* **1964**, *135*, 640−658.

(20) Murray, L. J.; Dincă, M.; Long, J. R. *Chem. Soc. Rev.* **2009**, *38*, 1294−1314.

(21) (a) Peterson, V. K.; Liu, Y.; Brown, C. M.; Kepert, C. J. *J. Am. Chem. Soc.* **2006**, *128*, 15578−15579. (b) Dincă, M.; Long, J. R *Angew. Chem., Int. Ed.* **2008**, *47*, 6766−6779. (c) Lin, X.; Telepeni, I.; Blake, A. J.; Dailly, A.; Brown, C. M.; Simmons, J. M.; Zoppi, M.; Walker, G. S.; Thomas, K. M.; Mays, T. J.; Hubberstey, P.; Champness, N. R.; Schröder, M. *J. Am. Chem. Soc.* **2009**, *131*, 2159−2171.

(22) Chen, B.; Ockwig, N. W.; Millward, A. R.; Contreras, D. S.; Yaghi, O. M. *Angew. Chem., Int. Ed.* **2005**, *44*, 4745−4749.

(23) Dincă, M.; Yu, A. F.; Long, J. R. *J. Am. Chem. Soc.* **2006**, *128*, 8904−8913.

(24) Dincă, M.; Dailly, A.; Liu, Y.; Brown, C. M.; Neumann, D. A.; Long, J. R. *J. Am. Chem. Soc.* **2006**, *128*, 16876−16883.

(25) Han, S. S.; Furukawa, H.; Yaghi, O. M.; Goddard, W. A. III *J. Am. Chem. Soc.* **2008**, *130*, 11580−11581.

(26) Rosi, N. L.; Eckert, J.; Eddaoudi, M.; Vodak, D. T.; Kim, J.; O'Keefee, M.; Yaghi, O. M. *Science* **2003**, *300*, 1127−1129.

(27) Li, Y. W.; Yang, R. T. *J. Am. Chem. Soc.* **2006**, *128*, 726−727.

(28) (a) Jhung, S. H.; Toon, J. W.; Kimand, H. K.; Chang, J.-S. *J. Phys. Chem. B* **2006**, *110*, 9371−9374. (b) Jhung, S. H.; Toon, J. W.; Kim, H. K.; Chang, J.-S. *Bull. Korean Chem. Soc.* **2005**, *26*, 1075−1078.

(29) Rowsell, J. L. C.; Yaghi, O. M. *Microporous Mesporous Mater.* **2004**, *73*, 3−14.

(30) (a) Latroche, M.; Surblé, S.; Serre, C.; Mellot-Draznieks, C.; Llewellyn, P. L.; Lee, J.-H.; Chang, J.-S.; Jhung, S. H.; Férey., G. *Angew. Chem., Int. Ed.* **2006**, *45*, 8227−8231. (b) Furukawa, H.; Millerb, M. A.; Yaghi, O. M. *J. Mater. Chem.* **2007**, *17*, 3197−3204.

(31) Plant, D. F.; Maurin, G.; Deroche, I.; Llewellyn, P. L. *Microporous Mesoporous Mater.* **2007**, *99*, 70.

(32) Dietzel, P. D. C.; Johnsen, R. E.; Fjellvag, H.; Bordiga, S.; Groppo, E.; Chavanc, S.; Blom, R. *Chem. Commun.* **2008**, 5125−5127.